This article has been accepted for inclusion in a future issue of this journal. Content is final as presented, with the exception of pagination.

IEEE Journal of Microwaves

Received 3 October 2024; revised 7 March 2025 and 31 May 2025; accepted 31 May 2025.

Digital Object Identifier 10.1109/JMW.2025.3576358

Electro-Optic Co-Simulation in High-Speed Silicon Photonics Transceiver Design Using Standard Electronic Circuit Simulator

KEISUKE KAWAHARA (Member, IEEE) AND TOSHIHIKO BABA (Fellow, IEEE)

Department of Mathematics, Physics, Electrical Engineering and Computer Science, Yokohama National University, Yokohama 240-8501, Japan

CORRESPONDING AUTHOR: Keisuke Kawahara (e-mail: keisuke@ieee.org).

This work was supported by JSPS KAKENHI under Grant JP23KJ0988.

ABSTRACT The increasing demand for high-speed optical interconnects requires the integration of photonics and electronics, with electro-optic (EO) co-simulation being crucial. However, fragmented electronic/photonic simulators and incomplete models, which do not include the radio-frequency characteristics and noise, are still prevalent, and thus, an EO co-simulation environment for high-speed transceiver design has not yet been established. Here, we present a unified and experimentally validated EO co-simulation library that enables accurate transmission performance predictions at symbol rates exceeding 50 Gbaud. Specifically, we model passive photonic components, such as waveguides and couplers, as well as two types of Si Mach–Zehnder modulators, incorporating frequency-dependent lossy traveling-wave electrodes and slow-light enhancement. We also show models for test equipment with validated noise characteristics, including an erbium-doped fiber amplifier (EDFA), a tunable filter, and a photodetector module, to construct a full optical link testbench. The S-parameter simulations agreed well with measurements up to 40 GHz, and the signal transmission simulations matched measurements up to 64 Gbps. All models and sample testbenches are available on GitHub.

INDEX TERMS Circuit simulation, integrated circuit modeling, high-speed integrated circuits, optical interconnections, silicon photonics, microwave photonics, optical modulators, electro-optic modulators, photonic integrated circuits, photonic crystals, slow light, erbium-doped fiber amplifiers.

I. INTRODUCTION

The exponential growth of demand in data centers and high-performance computers requires high-speed optical interconnects. Terabit Ethernet requires symbol rates exceeding 50 Gbaud and compact form factors to meet this demand [1]. Integrating photonics and electronics addresses these requirements by minimizing connection losses and reducing the footprint [2], [3], [4], [5], [6], [7], [8]. Due to the high cost of photomasks and long lead times in silicon (Si) photonics manufacturing, accurate electro-optic (EO) co-simulation is essential to predicting the performance of designed devices. However, existing simulators for electronics and photonics are fragmented, and the design process often involves inefficient manual data exchange. An effective approach is to perform co-simulation in an integrated environment, and attempts have been made to implement photonic device models in electronic circuit simulators like Synopsys, Cadence, and Keysight using Verilog-A [9]. Earlier studies established the theoretical foundation for simulating optical propagation in electronic circuit simulators by using equivalent baseband models [10], [11], [12], [13], [14], [15], [16]. However, they did not include practical models that reflect real device characteristics. Various physical effects, such as optical losses, back reflection, nonlinearity, high-frequency response, and noise, must be captured and experimentally validated for practical design. Subsequent studies modeled individual photonic components, such as passive photonic components [17], [18], [19], [20], [21], [22], optical modulators [23], [24], [25], [26], and photodetectors (PDs) [27], incorporating the real device characteristics, but these models were developed separately and were not integrated into a unified library. To our knowledge, the most advanced photonic model library is GlobalFoundries' Fotonix technology [28]. However, Si MZM-based optical link simulations report a maximum symbol rate of only 26.5 Gbaud.

© 2025 The Authors. This work is licensed under a Creative Commons Attribution 4.0 License. For more information, see https://creativecommons.org/licenses/by/4.0/

This article has been accepted for inclusion in a future issue of this journal. Content is final as presented, with the exception of pagination.

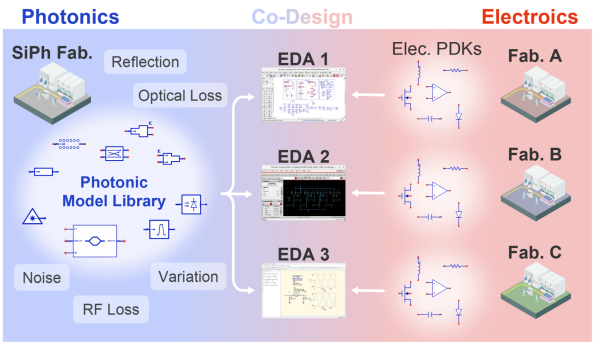


FIGURE 1. Concept of EO co-design using interoperable photonic device models and electronic circuit simulators. The model's interoperability allows any combination of photonics and electronics foundries.

Moreover, these models lack noise characterization, making them unsuitable for realistic performance evaluation in the next-generation 800-Gbps or 1.6-Tbps systems. Furthermore, the details of the reported models are largely undisclosed, hindering the progress of this type of research. Thus, an EO co-simulation environment supporting accurate high-speed transceiver design has not yet been established, making it necessary to develop a unified and experimentally validated co-simulation library and disclose its details.

In this study, we developed an experimentally validated EO co-simulation library with accurate photonic device models that predict transmission performance at symbol rates exceeding 50 Gbaud, with all details and source codes publicly disclosed. Specifically, we modeled passive photonic components, including waveguides and couplers, as well as two types of Si Mach-Zehnder optical modulators. The modulators incorporate frequency-dependent lossy traveling-wave electrodes and leverage the slow-light enhancement of photonic crystal waveguides (PCW). In addition, we developed models for test equipment with validated noise characteristics, including an erbium-doped fiber amplifier (EDFA), a tunable filter, and a photodetector module, and constructed a full optical link test bench. Implemented in Verilog-A, the library ensures interoperability across various simulation tools and enables co-design with both photonics and electronics foundries, as shown in Fig. 1.

In this paper, Section II presents the full process of Si photonic device modeling, and Section III describes the modeling of the test equipment for accurate noise level estimation. Section IV demonstrates EO co-simulation with a developed testbench, validated up to 64 Gbaud. All models and sample testbenches in Keysight's Advanced Design System (ADS) are available on GitHub [29].

II. SI PHOTONICS COMPONENTS

In this section, Si photonics component models are developed, targeting a CMOS-compatible 300-mm silicon-on-insulator wafer process developed by the National Institute of Advanced Industrial Science and Technology. The simulation is based on the equivalent baseband model [12]. Section III-A briefly reviews the simulation principles through a description of the waveguide model. Section III-B introduces coupler models for optical splitting, combining, and loopback. Section III-C details two types of Si Mach-Zehnder modulator models with validated high-frequency responses and slow-light enhancement.

A. WAVEGUIDE

The difficulty in introducing photonic devices into electronic circuit simulations is that the frequency of the optical carrier, ω_O, is much higher than that of the electrical signal, which requires a very large sampling rate. For example, for a wavelength of $\lambda = 1550$ nm, $f = \omega_O/2\pi = 193$ THz. To address this difficulty, equivalent baseband simulations were introduced. Here, ω_O is shifted by a reference frequency, $\omega_{ref} = 2\pi c/\lambda_{ref}$. The electric field of the optical signal is expressed as

$$\tilde{E}_B(t) = \exp(-j\omega_{ref}t)\,\tilde{E}(t), \tag{1}$$

where $\tilde{E}(t)$ is the analytic signal [30] of the electric field $E(t)$. Typically, ω_{ref} is approximated by ω_O. For example, the electric field of continuous wave laser light is represented as

$$\tilde{E}_{LD}(t) = A_{LD}\exp\left[j(\omega_o - \omega_{ref})t\right], \tag{2}$$

where A_{LD} is the amplitude of the electrical field. To support complex numbers and bidirectional propagation in circuit simulators, bus wires $E[0{:}3]$ are used, where $E[0]$ and $E[1]$ represent the real and imaginary parts of forward propagation and $E[2]$ and $E[3]$ represent those of backward propagation, respectively. The propagation of light in a waveguide is modeled as

$$\tilde{E}_{out} = \exp\left[-\left(\frac{\alpha}{2} + \frac{j\omega_{ref}n_{eq}}{c}\right)l_{wg}\right]\tilde{E}_{in}\left(t - \frac{n_g}{c}l_{wg}\right), \tag{3}$$

where n_{eq}, α, n_g, and l_{wg} represent modal equivalent refractive index, loss constant, group index, and waveguide length, respectively. A Si wire waveguide typically has $n_{eq} = 2.31$, $n_g = 4.34$, $\alpha = 2$ dB/cm for the transverse-electric (TE) polarization at $\lambda = 1550$ nm. Listing 1 shows a sample Verilog-A model for a waveguide, based on [12]. The Polar2Cartesian() function converts polar coordinates to Cartesian coordinates, and the CartesianMultiplier() function computes the product of complex numbers, as described in Appendix 1. The group delay expressed in (1) is implemented by the absolute delay operator absdelay() predefined in Verilog-A.

B. COUPLER

The couplers are used to split, combine, and loopback the light. Different models are used to match the forward and backward propagation definitions of the input and output ports for each application. The one-by-two couplers are dominated by

$$\begin{pmatrix}\tilde{E}_{o1}\\ \tilde{E}_{o2}\end{pmatrix} = \begin{pmatrix}\sqrt{\kappa}\\ \sqrt{1-\kappa}\end{pmatrix}\tilde{E}_{in}, \tag{4}$$

This article has been accepted for inclusion in a future issue of this journal. Content is final as presented, with the exception of pagination.

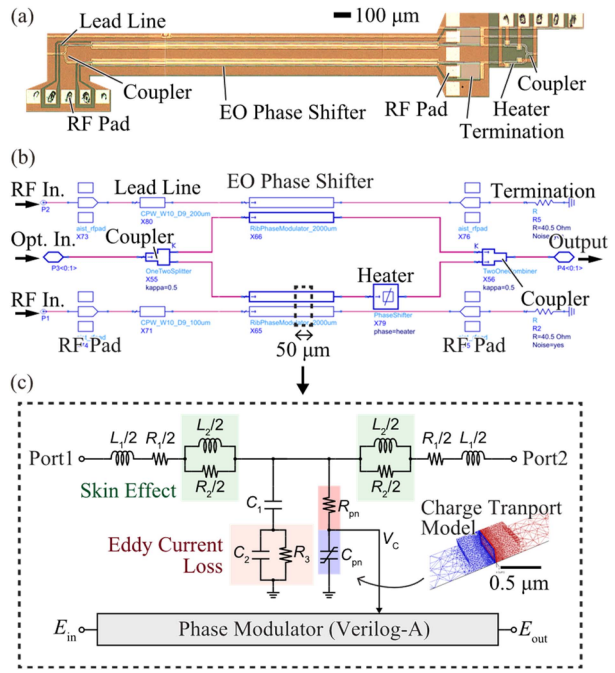


FIGURE 2. Modeling of Si rib-waveguide Mach-Zehnder modulator. (a) Optical micrograph of fabricated device. (b) Model schematic. (c) Subcircuit of the segment of the traveling-wave electrodes.

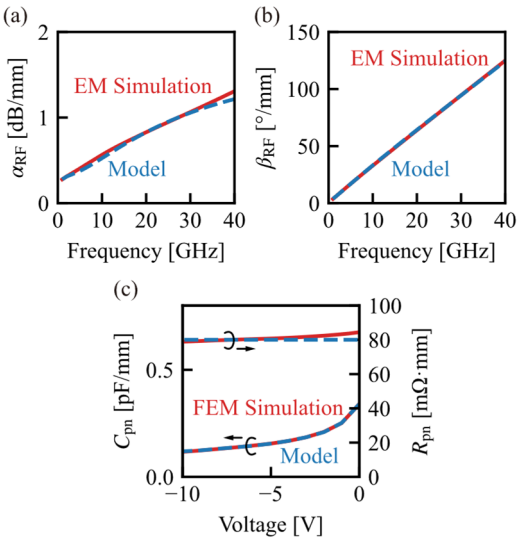


FIGURE 3. Fitting of the electrical parameters. (a) RF loss constant. (b) RF phase constant. (c) Capacitance and resistance of the p-n junction.

$$\tilde{E}_{\text{out}} = \begin{pmatrix} \sqrt{\kappa} & \sqrt{1-\kappa} \end{pmatrix} \cdot \begin{pmatrix} \tilde{E}_{\text{i1}} \\ \tilde{E}_{\text{i2}} \end{pmatrix}, \tag{5}$$

where κ is the coupling power ratio. See Listings 2 and 3 for sample codes of these models. For a two-by-two (directional) coupler, which is dominated by

$$\begin{pmatrix} \tilde{E}_{\text{o1}} \\ \tilde{E}_{\text{o2}} \end{pmatrix} = \begin{pmatrix} \sqrt{1-\kappa} & -j\sqrt{\kappa} \\ -j\sqrt{\kappa} & \sqrt{1-\kappa} \end{pmatrix} \cdot \begin{pmatrix} \tilde{E}_{\text{i1}} \\ \tilde{E}_{\text{i2}} \end{pmatrix} \quad [31]. \tag{6}$$

The couplers typically have an excess loss of about 0.5 dB. This loss is modeled by connecting the optical attenuator (Listing 4) to the input and output ports of the coupler.

C. RIB WAVEGUIDE MACH-ZEHNDER MODULATOR

Mach-Zehnder optical modulators are particularly difficult to model because they require accurate knowledge of RC time constants, RF losses, optical and electrical group delays, and characteristic impedance of the electrode. For this reason, most Verilog-A models of Mach-Zehnder modulators are limited to 25 Gbaud due to low accuracy in fitting RF characteristics [25], [26]. Fig. 2(a) and (b) show the optical micrograph and developed model of the rib-type Mach-Zehnder modulator. The input light is split at the coupler and passes through the EO phase shifter. A thermo-optic heater adjusts the bias phase between the arms. The RF signals are input from the RF pads, propagate through the traveling-wave electrodes of the EO phase shifters, and are terminated with the resistors. The equivalent circuit model of the EO phase shifter is shown in Fig. 2(c). In this study, we incorporated the skin effect in the metal wiring and eddy currents in the substrate into the model. L_1 and R_1 are the wiring inductance and resistance, respectively. L_2 and R_2 model the increase in parasitic resistance at high frequencies due to the skin effect. C_1 represents the substrate capacitance, and C_2 and R_3 model the reduction in shunt impedance at high frequencies due to eddy currents. These parameters were extracted by electromagnetic analysis using Keysight's Momentum. R_{pn} and C_{pn} are the junction resistor and capacitor at the pn junction, which were extracted by a charge transport simulation using Ansys's Lumerical. C_{pn} has a voltage dependency due to the expansion of the depletion layer, which is modeled by a polynomial function for the applied voltage V_{C}. The phase shifter is driven by V_{C}, changing the mode equivalent refractive index n_{eq} and optical loss α as follows:

$$n_{\text{eq}} = n_0 + n_1 V_{\text{in}} + n_2 V_{\text{in}}^2 \cdots, \tag{7}$$

$$\alpha = \alpha_0 + \alpha_1 V_{\text{in}} + \alpha_2 V_{\text{in}}^2 \cdots, \tag{8}$$

where n_0 and α_0 represent the equivalent index and optical loss without applied voltage. n_1, n_2, α_1, and α_2 denote the first- and second-order coefficients of n_{eq} and α, respectively, with respect to V_{in}. The traveling-wave electrodes with a length of 2.0 mm were modeled by connecting 40 segments with a length of 50 μm in series. This distributed model accurately simulates the RF propagation losses, impedance mismatch, and phase mismatch between the optical and RF signals. Fig. 3(a) and (b) show the fitting results of the RF propagation constants of the electrodes, $\gamma_{\text{RF}} = \alpha_{\text{RF}} + j\beta_{\text{RF}}$, which can be calculated from the S-parameters as follows:

$$e^{-\gamma_{\text{RF}} l} = \left(\frac{1 - S_{11}^2 + S_{21}^2}{2S_{21}} \pm K \right)^{-1} \quad [32], \tag{9}$$

This article has been accepted for inclusion in a future issue of this journal. Content is final as presented, with the exception of pagination.

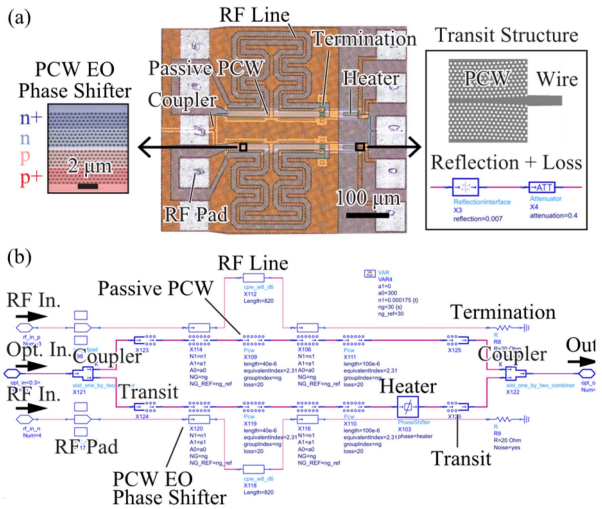


FIGURE 4. Modeling of a Si PCW Mach-Zehnder modulator. (a) Micrograph of the modulator and transition structure between the PCW and thin wire. The transition was modeled by optical reflections and attenuators (loss). (b) Model schematic. Similar to the rib type, the EO phase shifter model consists of subcircuits of the segmented traveling-wave electrode.

where

$$K = \sqrt{\frac{\left(S_{11}^2 - S_{21}^2 + 1\right)^2 - \left(2S_{11}^2\right)}{(2S_{21})^2}}. \tag{10}$$

By properly accounting for skin effects and eddy current losses, good fits were obtained up to 40 GHz for γ_{RF}. In addition, the voltage dependency of C_{pn} is properly modeled as shown in Fig. 3(c), which enables accurate simulation of the frequency response.

C. PCW MACH-ZEHNDER MODULATOR

Fig. 4(a) and (b) show the optical micrograph and model of the Si PCW Mach-Zehnder modulator. The slow light effect generated in the PCW enhances the light-matter interaction, and the phase shift in the PCW, $\Delta\varphi$, is increased in proportion to n_{g}, as follows:

$$\Delta\phi = k_0 n_g \frac{\Delta n_{\mathrm{eq}}}{n_{\mathrm{eq}}} \zeta l_{\mathrm{pcw}} \quad [33], \tag{11}$$

where Δn_{eq}, l_{pcw}, and ζ represent the change in n_{eq}, the phase shifter length, and a constant value, respectively. Listing 5 shows the model of the PCW phase shifter. In this model, the first-order voltage coefficient of the refractive index, n_1, was replaced by $(n_{\mathrm{g}}/n_{\mathrm{g_ref}})n_1$ to simulate the slow light enhancement, where $n_{\mathrm{g_ref}}$ is n_{g} without a significant slow light effect. The typical frequency bandwidth for slow light ranges from several nm to tens of nm, with an n_{g} dispersion of 10–100. However, since the RF signal bandwidth is around 50 GHz, the group velocity dispersion within the signal bandwidth is sufficiently small and does not have a significant effect. For example, at a center wavelength of 1550 nm, a 50-GHz RF bandwidth is approximately 0.4 nm, which is much smaller than the dispersion effects of slow light. Therefore, applying n_{g} to the voltage-dependent first-order coefficient of the refractive index is sufficient to capture the slow-light enhancement. In applications where the optical filter characteristics of the PCW need to be calculated, a more detailed model may be required. To improve the phase matching between slow light and RF signals, the phase shifter was divided into two segments, and RF delay lines were inserted between them [34]. The RF lines were modeled by using the transmission line predefined in ADS. Undoped passive PCWs are placed between the phase shifter segments to electrically separate each segment. To properly account for the optical delay due to the passive PCWs, we inserted a waveguide into the model. The model parameters were extracted based on device simulations in the same manner as those for the rib-waveguide modulator. Optical reflectors (Listing 6) with a reflectivity of 7.5% were inserted at the input and output of the PCW, and the connection structure was modeled.

III. TESTING EQUIPMENT

In this section, we develop models for testing equipment to construct a receiver composed of an EDFA, tunable filter, and photodetector module. Our model introduces noise, which has a significant impact on the bit error rate and has been overlooked in traditional EO co-simulation. Here, we measure and model the noise of each device used in our lab to improve the accuracy of our simulations.

A. EDFA

EDFAs compensate for transmission losses and increase receiver sensitivity, but amplified spontaneous emission (ASE) introduces noise that must be modeled. The input power is amplified by G_{EDFA} and then ASE, approximated by Gaussian noise, is added. The noise power level, P_{ASE}, is given by

$$P_{ASE} = \mu h\nu \Delta\nu \left(G_{\mathrm{EDFA}} - 1\right), \tag{12}$$

where μ is the inversion factor, $h\nu$ is the photon energy, and $\Delta\nu$ is the frequency bandwidth [35]. Fig. 5(a) and (b) show the measurement setup and measured output spectrum of an EDFA (Alnair Labs' CPA-100-CL). When the output power is controlled at a constant value, a smaller P_{in} results in a larger G_{EDFA} and a larger P_{ASE}. The power spectral density, PSD_{ASE}, can be calculated from the wavelength resolution of the optical spectrum analyzer, $\lambda_{\mathrm{res}} = 0.5$ nm. Fig. 5(c) compares the measurement and model of PSD_{ASE} for $(G_{\mathrm{EDFA}} - 1)$. The coefficient $\mu h\nu\Delta\nu$ was determined to be 3.44×10^{-19} W/Hz by the least-squares method. The noise bandwidth in the simulation is equal to the sampling frequency of the simulation, i.e., $\Delta\nu = f_{\mathrm{s}}$. Listing 7 shows the Verilog-A code of the EDFA. A Gaussian random function \$rdist_normal() was used for noise generation, with the standard deviation set to be the square root of the noise power.

B. TUNABLE FILTER

Optical filters are used to remove ASE generated by the EDFA. As mentioned earlier, the optical frequency is shifted

This article has been accepted for inclusion in a future issue of this journal. Content is final as presented, with the exception of pagination.

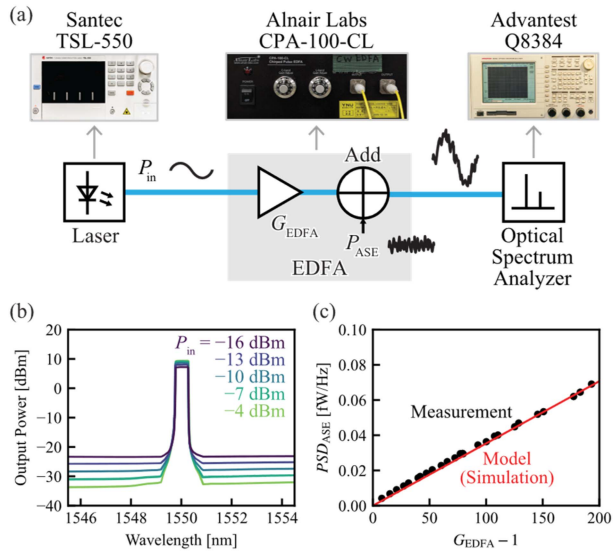


FIGURE 5. Modeling of an EDFA. (a) Experimental setup for noise modeling of the EDFA and block diagram of the model. (b) Measured power spectrum output from the EDFA. (c) Measured and simulated power spectral densities of the ASE.

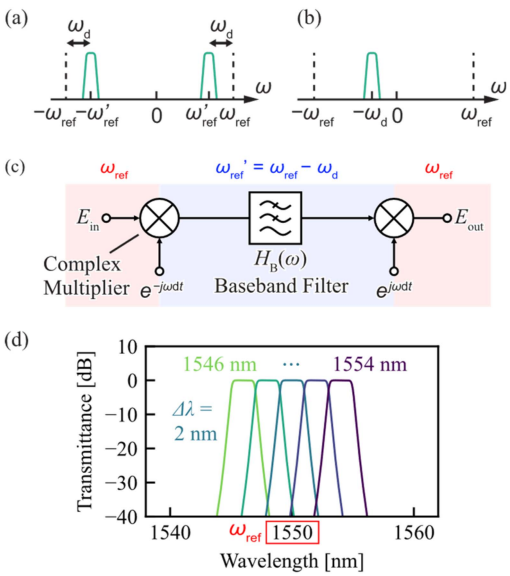


FIGURE 6. Modeling of a tunable filter. (a) Frequency response of optical bandpass filter. (b) Frequency response of frequency-shifted equivalent filter. (c) Block diagram of the model. (d) Simulated transmission spectrum.

to the baseband by ω_{ref} to reduce the number of time steps in the transient analysis. Consequently, the frequency response of the filter must also be shifted accordingly. Fig. 6(a) and (b) show the responses of the bandpass filter before and after the frequency shift, respectively. The center frequency of the filter must be adjustable to any value other than ω_{ref}. We express the difference between ω_{ref} and the center frequency of the filter as ω_d. This causes the frequency response of the baseband-equivalent filter to become asymmetric around 0

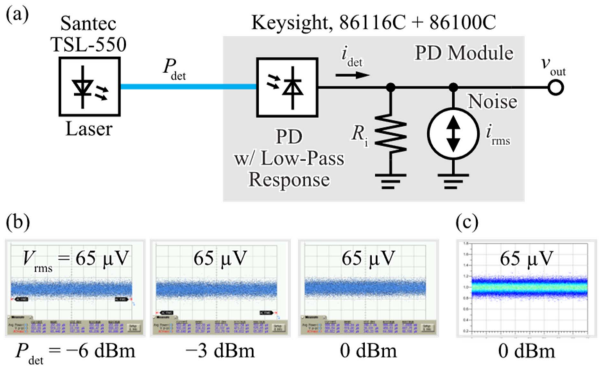


FIGURE 7. Modeling of a photodetector module. (a) Experimental setup for noise modeling of the module and block diagram of the model. (b) Measured noise waveform of Keysight's 86116C photodetector module. (c) Simulated noise waveform.

Hz, resulting in complex coefficients in the Laplace transfer function. Since Verilog-A does not natively support complex numbers, our model locally adjusts the reference frequency. Fig. 6(c) shows a block diagram of the tunable filter. In the time domain, the frequency shift corresponds to a multiplication by $\exp(-j\omega_d t)$, so the tunable filter is implemented by inserting a complex multiplier before and after the baseband low-pass filter. Listing 8 shows the Verilog-A code for the tunable filter. The center wavelength is specified by the parameter 'wavelength'. 'osc1' and 'osc2' serve as local oscillators for converting the reference frequency at both the input and output. The baseband low-pass filter was implemented using the laplace_nd() function predefined in Verilog-A. The coefficients of the Laplace transfer function were determined by a MATLAB script and are provided as an array. The filter response was approximated using a sixth-order Butterworth filter, which offers a flat passband with minimal impact on the signal and sufficient roll-off to eliminate ASE. The optical bandwidth, $\Delta\lambda$, was set to 2 nm. Fig. 6(d) shows the simulated transmission spectrum. The center wavelength was varied from 1546 nm to 1554 nm in 2 nm increments, with λ_{ref} fixed at 1550 nm, demonstrating the wavelength tuning operation.

C. PHOTODETECTOR MODULE

The photodetector module consists of a photodiode (PD), a trans-impedance amplifier (TIA), and an analog-to-digital converter (ADC). The PD outputs a current $i_{det} = R \cdot P_{det}$, with the received power, P_{det}, and the responsivity of the PD, R. The RC time constant at the PD was introduced into the model by a first-order low-pass transfer function using the laplace_nd() function. In addition, we introduced the thermal noise from the TIA and ADC. Fig. 7(a) shows the measurement setup and corresponding model of the PD module (Keysight's 86116C). The TIA was replaced by a load resistor R_L. The TIA noise and ADC noise are modeled by the thermal noise generated by R_L. The root-mean-squared (RMS) voltage

This article has been accepted for inclusion in a future issue of this journal. Content is final as presented, with the exception of pagination.

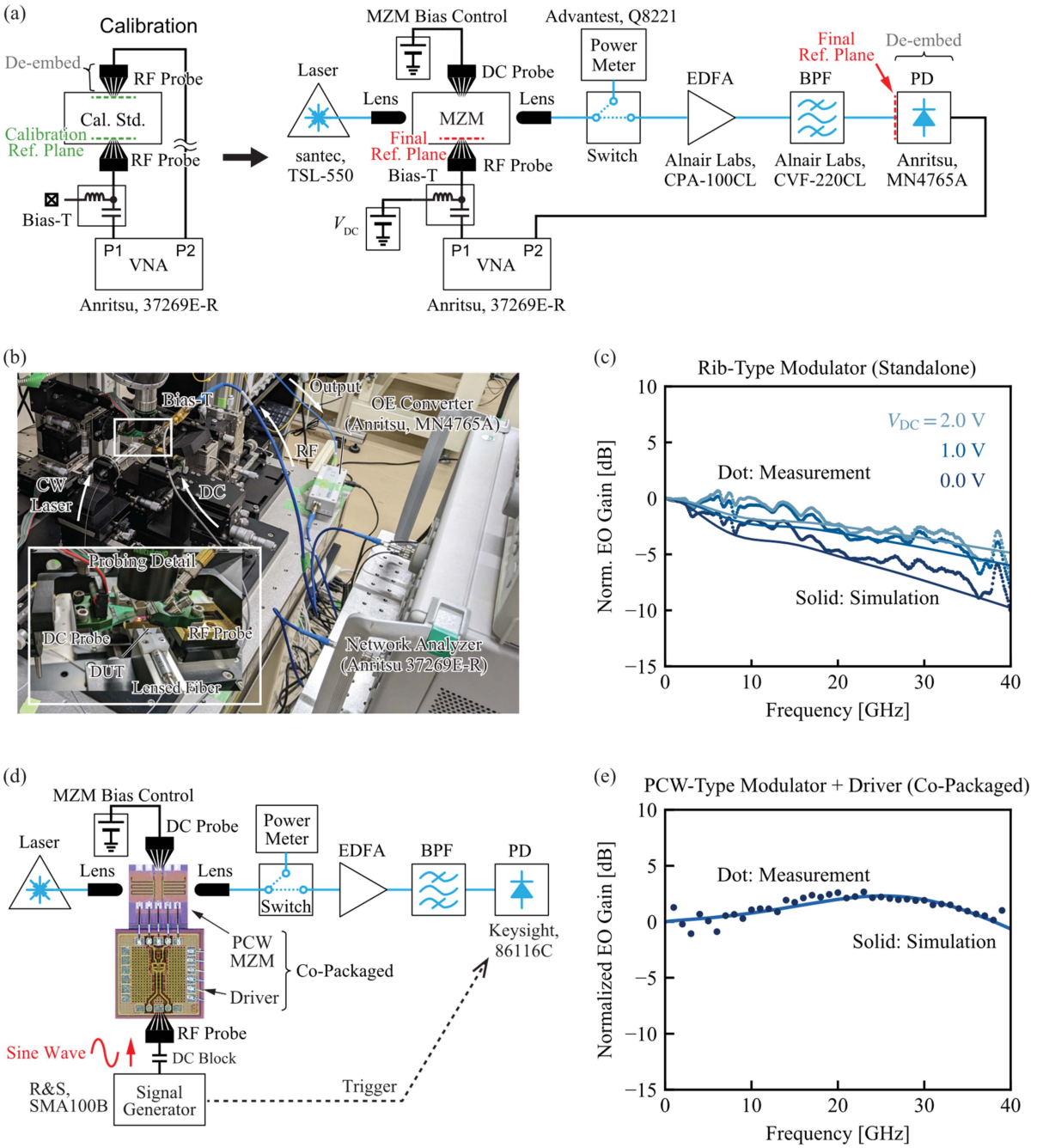


FIGURE 8. **Experimental validation of the frequency responses of the Si optical modulators. (a) Experimental setup for S-parameter measurement using a VNA with a calibration step. (b) Photograph of the setup. (c) Measured and simulated EO gain of the standalone rib-type modulator with different bias voltages. (d) Experimental setup for EO gain measurement using a signal generator. (e) Measured and simulated EO gain of co-packaged transmitter module with a PCW-type modulator and driver.**

of the thermal noise, V_{rms}, is given by

$$V_{\mathrm{rms}} = \sqrt{4kTR_LB}, \tag{13}$$

where k, T, and B represent the Boltzmann constant, absolute temperature, and bandwidth, respectively. Fig. 7(b) shows the measured noise waveforms when P_{det} was varied from negative infinity to 0 dBm. The measured RMS voltage was $V_{\mathrm{rms}} = 65\ \mu$V. The fact that V_{rms} is independent of P_{det} suggests that the primary sources of noise are the TIA and ADC, rather than the shot noise of the photodiode. From (13), R_{L} was determined to be 0.1 Ω to produce thermal noise with $V_{\mathrm{rms}} = 65\ \mu$V. Here, $T = 27$°C and $B = 2500$ GHz were used

This article has been accepted for inclusion in a future issue of this journal. Content is final as presented, with the exception of pagination.

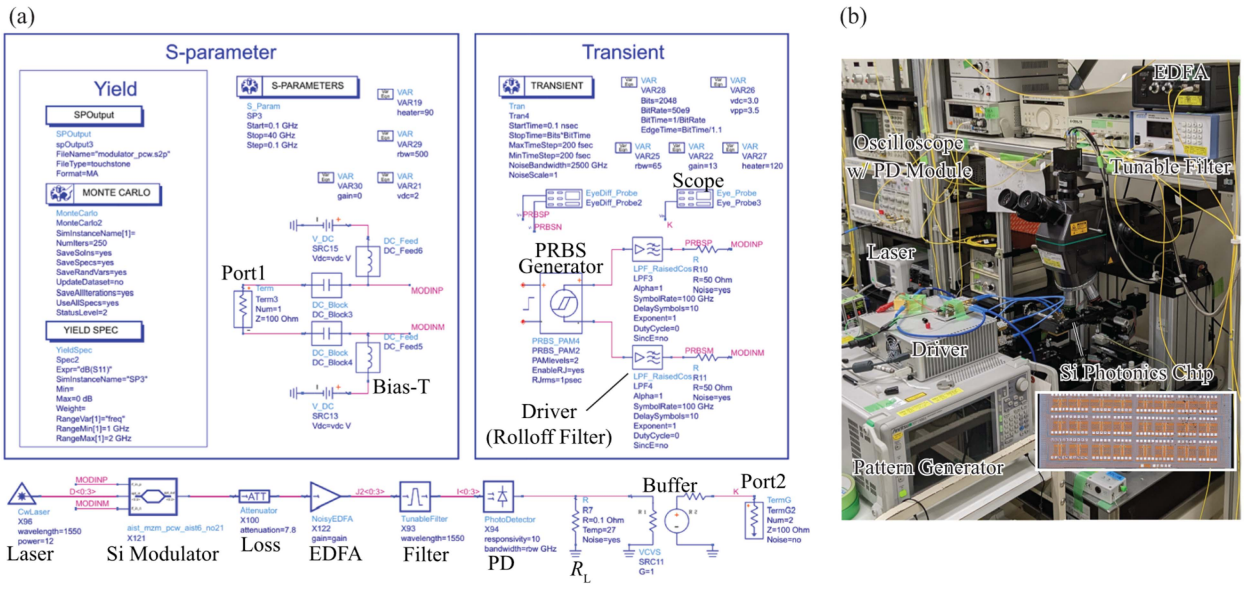


FIGURE 9. Experimental validation of the full optical link. (a) Testbench for signal transmission constructed in ADS. (b) Experimental setup for >50-Gbaud signal transmission.

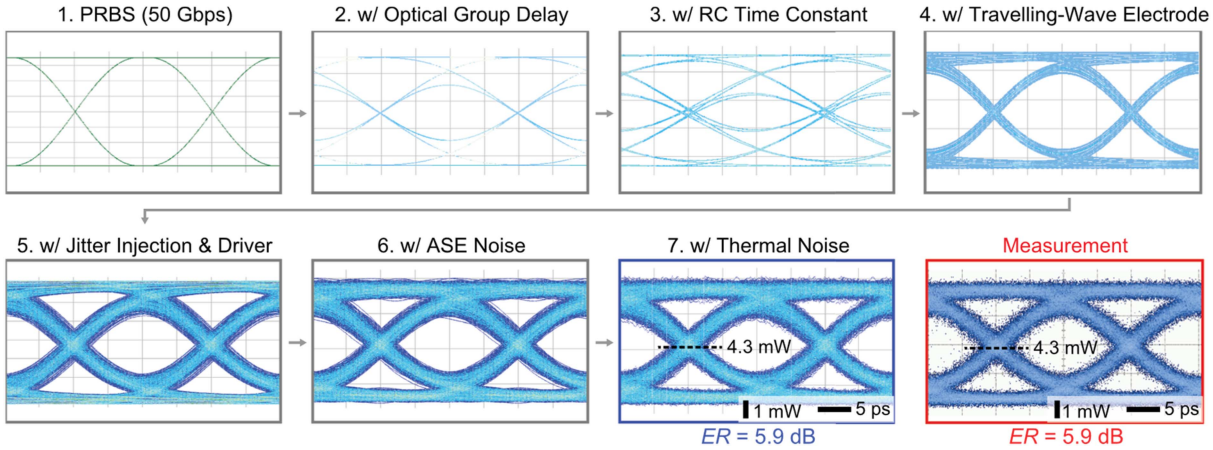


FIGURE 10. Simulated and measured eye diagrams for the rib-type Mach–Zehnder modulator at 50 Gbaud. The simulated eye diagrams show the sequential changes due to the addition of physical properties.

by setting parameters "Temp" and "NoiseBandwidth" in the resistor model of ADS. The responsivity R was set to 10 so that the output power is directly displayed as a voltage. As shown in Fig. 7(c), the simulated noise amplitude was $V_{\mathrm{rms}} = 65\ \mu$V, which was consistent with the measurement.

IV. EXPERIMENTAL VALIDATION

A. FREQUENCY RESPONSES

We evaluated the EO S-parameters of the modulator. Fig. 8(a) shows the experimental setup. We used a vector network analyzer (VNA: Anritsu, 37269E-R) and a PD module (Anritsu, MN4765A). The VNA was calibrated using a calibration standard substrate, as shown on the left side of Fig. 8(a), with the calibration reference planes placed at the probe tips. The output RF probe was de-embedded after measurement because it was used only for the calibration step. Then, EO S-parameters were measured using the setup shown on the right side of Fig. 8(a). The frequency response of the PD module was de-embedded using the S-parameters provided by Anritsu. The final reference planes are indicated by the red dashed line in Fig. 8(a). We used an EDFA and a BPF to obtain a sufficient signal-to-noise ratio, which did not affect the frequency response, allowing us to accurately capture the device characteristics. Fig. 8(b) shows a photograph of the experimental setup with the probing details. Fig. 8(c) shows the measured and simulated frequency responses of the standalone rib-waveguide modulator for various bias voltages V_{DC}. The simulated responses (solid lines) roughly agreed

This article has been accepted for inclusion in a future issue of this journal. Content is final as presented, with the exception of pagination.

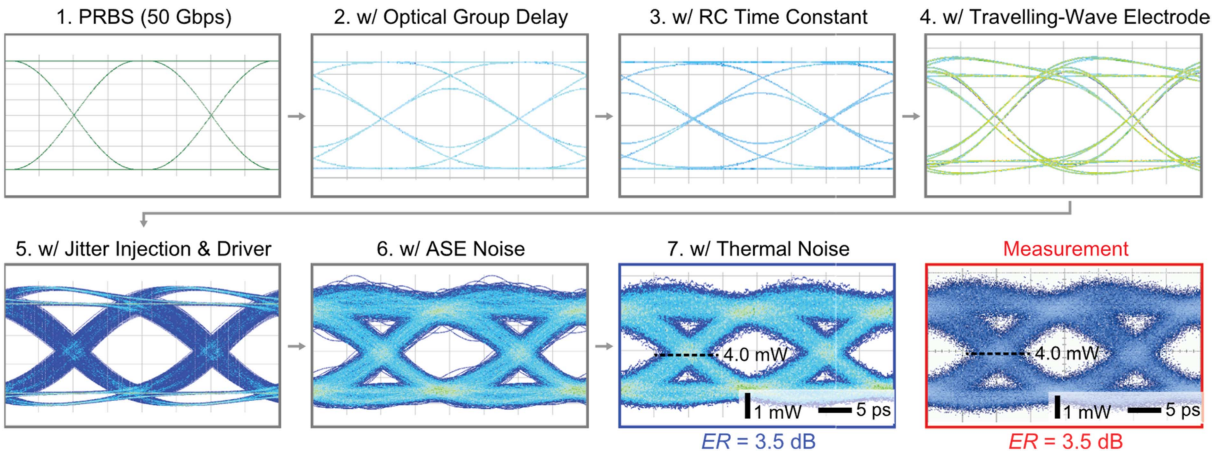


FIGURE 11. Simulated and measured eye diagrams for the PCW-type Mach-Zehnder modulator at 50 Gbaud. The simulated eye diagrams show the sequential changes due to the addition of physical properties.

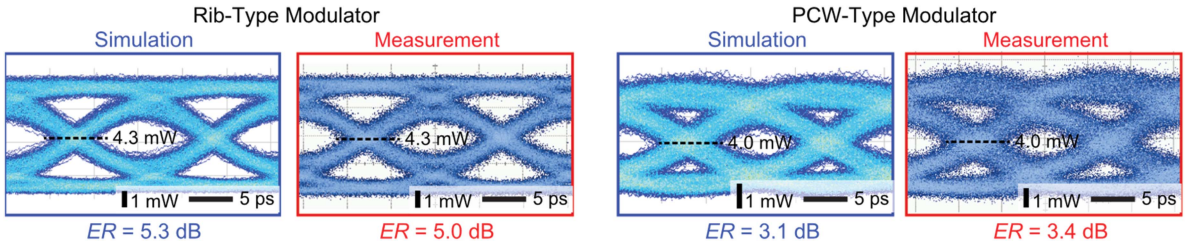


FIGURE 12. Simulated and measured eye diagrams for the rib- and PCW-type Mach–Zehnder modulator at 64 Gbaud.

with the measurements (dots) from DC to 40 GHz. We observed approximately 1-dB gaps between the measurements and simulations below 20 GHz, as well as peaks at 38 GHz that did not appear in the simulations. As explained above, during calibration and EO S-parameter measurement, it was necessary to reconnect the wiring on port 2, and bending the RF cable could have changed its S-parameters and caused calibration errors [36], [37]. Therefore, these discrepancies do not indicate any issues with the device or the model. The high accuracy of the model is attributed to the careful incorporation of RF loss, EO phase mismatch, impedance mismatch, RC time constant, and the nonlinearity of C_{pn}.

We further fabricated an optical transmitter module in which a PCW modulator and driver were co-packaged, and we measured its frequency response. The driver was designed using a 130-nm BiCMOS process through EO co-simulation. The BiCMOS technology model was provided by the foundry (Innovations for High Performance Microelectronics, IHP). The design details are described in [38]. Fig. 8(d) shows the experimental setup. To prevent calibration errors, we used a signal generator (Rohde & Schwarz, SMA100B) for this measurement. A sinusoidal signal with a peak-to-peak amplitude of 100 mV was applied to the driver, and the optical modulation amplitude was measured using a sampling oscilloscope (Keysight, 86116C + 86100C). The measured frequency ranged from 1 GHz to 40 GHz in 1 GHz steps. The losses of the input cables and probes were de-embedded after the measurement. As shown in Fig. 8(e), the measured and co-simulated EO gain showed good agreement up to 40 GHz. In this measurement, the gap observed when using the VNA was not present. These results suggest that our co-simulation model library enables highly accurate design of co-packaged transceivers.

B. EYE DIAGRAMS

Then, we built a simulation test bench corresponding to the experimental setup using the developed model library, as shown in Fig. 9, and verified the accuracy of the models. CW light output from a tunable laser source (Santec's TSL-550) was input to a Si optical modulator. The modulated light passed through an EDFA (Alnair Labs' CPA-100-CL) and bandpass filter (Alnair Labs' CVF-220CL). The eye diagrams were observed by a sampling oscilloscope equipped with a photodetector module (Keysight's 86116C, 86100C) while driving the modulator using a broadband amplifier (SHF's S804B). The pseudorandom bit sequence (PRBS) was generated by a pulse pattern generator (Anritsu's MP1800A) and a multiplexer (SHF's 601A). The RF loss in the cable was compensated for by an equalizer (SHF's EQ25A). The modulators were push-pull driven at $V_{\mathrm{pp}} = 3.5$ V. V_{DC} was set to -3 V for

This article has been accepted for inclusion in a future issue of this journal. Content is final as presented, with the exception of pagination.

the rib-type modulator and −1.75 V for the PCW-type modulator in both the simulation and the measurement. P_{LD} and P_{det} were set to 12 dBm and 5 dBm, respectively. In the simulation, all the components were replaced with our Verilog-A models or built-in electrical models in the simulator. The driver was replaced by a roll-off filter with a bandwidth of 50 GHz, and an RMS jitter of 1 ps was injected into the PRBS signal source, corresponding to the measurement. The modulation signals were 50- and 64-Gbps non-return-to-zero PRBS10 signals, and 2048 bits were transmitted at a fixed time step of 200 fs. The first 0.1 ns of the waveform was discarded to eliminate transients at the beginning of the simulation.

Figs. 10 and 11 show the results of 50-Gbaud signal transmission using rib-type and PCW-type modulators, respectively. In contrast to previously reported Verilog-A-based simulations, our simulations introduced physical properties that have a noticeable impact on signal quality in modulators and test equipment. These eye diagrams show the transitions as the various physical properties described in the modeling section were added. The optical group delay and the RC time constant of the modulator degrade the eye-opening. The traveling wave electrode improves eye-opening by matching the optical signal with the RF signal. Furthermore, the proper modeling of jitter and noise accurately simulated the measured waveform. Fig. 12 shows the measured and simulated eye diagrams at 64 Gbaud. The simulated results agreed well with the measurements under all conditions, with an error in extinction ratio (ER) of less than 1 dB. Therefore, the developed models enable precise prediction of transceiver link performance at high data rates exceeding 50 Gbaud, indicating their potential for designing 800G, 1.6T, and beyond.

V. CONCLUSION

In this study, we developed accurate and interoperable photonic device models that reflect the physical properties of fundamental Si photonic devices and equipment. We incorporated RF losses, optical losses, EO phase mismatch, impedance mismatch, and RC time constant into the models of Si rib waveguide and PCW Mach-Zehnder modulators. The S-parameter simulations showed good agreement with measurements up to 40 GHz, accurately predicting voltage dependency. In the signal transmission simulation, we incorporated all signal degradation factors present in the testing equipment, including jitter, ASE, and thermal noise. Consequently, the simulations accurately matched measurements up to 64 Gbps. These results facilitate precise verification and performance prediction of EO integrated circuits, paving the way for emerging applications.

APPENDIX

The key models that construct the testbench are shown in Listings 1 to 8. See the GitHub repository for the complete model library [29].

Listing 1: Verilog-A model of the waveguide (Waveguide.va).

```
module Waveguide(node1, node2);
    inout [0:3] node1;
    inout [0:3] node2;
    optical [0:3] node1, node2;
    optical [0:1] fwd, bwd, transfer_pol, transfer;

    parameter real length = 100e-6; // [m]
    parameter real equivalentIndex = 2.31;
    parameter real groupIndex = 4.34;
     parameter real loss = 2.0; // [dB/cm]
     real alpha = 23.0258509299404568 * loss;

     Polar2Cartesian Polar2Cartesian1(transfer_pol, transfer);

    // Forward and backward propagation
    CartesianMultiplier CartesianMultiplier1(transfer, node1[0:1], fwd[0:1]);
    CartesianMultiplier CartesianMultiplier2(transfer, node2[2:3], bwd[0:1]);

    analog begin
        // Propagation loss and phase rotation
        OptE(transfer_pol[0]) <+ exp(-alpha / 2 * length);
        OptE(transfer_pol[1]) <+ (-length * equivalentIndex * 2 * `M_PI * `F_REF / `P_C) % (2 * `M_PI);

        // Output
        OptE(node2[0]) <+ absdelay(OptE(fwd[0]), length * groupIndex / `P_C);
        OptE(node2[1]) <+ absdelay(OptE(fwd[1]), length * groupIndex / `P_C);
        OptE(node1[2]) <+ absdelay(OptE(bwd[0]), length * groupIndex / `P_C);
        OptE(node1[3]) <+ absdelay(OptE(bwd[1]), length * groupIndex / `P_C);
    end
endmodule
```

Listing 2: Verilog-A model of the one-by-two splitter (OneTwoSplitter.va).

```
module OneTwoSplitter(one, two1, two2); // one[0:1]:input, one[2:3]:output, two1[0:1]:output, two1[2:3]:input, two2[0:1]:output, two2[2:3]:input
    inout [0:3] one, two1, two2;
    optical [0:3] one, two1, two2;

    parameter real kappa = 0.5; // Power ratio

    analog begin
        OptE(two1[0]) <+ sqrt(kappa) * OptE(one[0]);
        OptE(two1[1]) <+ sqrt(kappa) * OptE(one[1]);
         OptE(two2[0]) <+ sqrt(1 - kappa) * OptE(one[0]);
         OptE(two2[1]) <+ sqrt(1 - kappa) * OptE(one[1]);
        OptE(one[2]) <+ OptE(two1[2]) * sqrt(kappa) + OptE(two2[2]) * sqrt(1 - kappa);
        OptE(one[3]) <+ OptE(two1[3]) * sqrt(kappa) + OptE(two2[3]) * sqrt(1 - kappa);
    end
endmodule
```

This article has been accepted for inclusion in a future issue of this journal. Content is final as presented, with the exception of pagination.

Listing 3: Verilog-A model of the one-by-two combiner (TwoOneCombiner.va).

```
module TwoOneCombiner(two1, two2, one);
    inout [0:3] two1, two2, one;
    optical [0:3] two1, two2, one;

    parameter real kappa = 0.5; // Power ratio

    analog begin
        OptE(one[0]) <+ OptE(two1[0]) * sqrt(kappa) + OptE(two2[0]) * sqrt(1 - kappa);
        OptE(one[1]) <+ OptE(two1[1]) * sqrt(kappa) + OptE(two2[1]) * sqrt(1 - kappa);
        OptE(two1[2]) <+ sqrt(kappa) * OptE(one[2]);
        OptE(two1[3]) <+ sqrt(kappa) * OptE(one[3]);
        OptE(two2[2]) <+ sqrt(1 - kappa) * OptE(one[2]);
        OptE(two2[3]) <+ sqrt(1 - kappa) * OptE(one[3]);
    end
endmodule
```

Listing 4: Verilog-A model of the optical attenuator (Attenuator.va).

```
module Attenuator(in, out);
    inout [0:3] in, out;
    optical [0:3] in, out;
    optical [0:1] transfer_pol, transfer;

    parameter real attenuation = 3.0; // [dB]

    Polar2Cartesian Polar2Cartesian1(transfer_pol, transfer);
    CartesianMultiplier CartesianMultiplier1(transfer, in[0:1], out[0:1]);
    CartesianMultiplier CartesianMultiplier2(transfer, out[2:3], in[2:3]);

    analog begin
        OptE(transfer_pol[0]) <+ pow(10, - attenuation / 20);
        OptE(transfer_pol[1]) <+ 0;
    end
endmodule
```

Listing 5: Verilog-A model of the PCW phase shifter (PcwPhaseModulator.va).

```
module PcwPhaseModulator(opt_in, opt_out, ele_in);
    inout [0:3] opt_in, opt_out; // Optical input and output
    input ele_in; // Electrical input
    optical [0:3] opt_in, opt_out, transfer_pol, transfer, out_tmp;
    optical [0:1] fwd, bwd, transfer_pol, transfer;
    electrical ele_in;

    parameter real length = 100e-6; // [m]
    parameter real equivalentIndex = 2.31; // at 0-V bias
    parameter real groupIndex = 20;
    parameter real refGroupIndex = 20;
    parameter real loss = 2.0; // [dB/cm] at 0-V bias

    real n0 = equivalentIndex;
    parameter real n1 = 0.0002;
    real a0 = 23.0258509299404568 * loss;
    parameter real a1 = 10;

    Polar2Cartesian Polar2Cartesian1(transfer_pol, transfer);
    CartesianMultiplier CartesianMultiplier1(transfer, opt_in[0:1], fwd);
    CartesianMultiplier CartesianMultiplier2(transfer, opt_out[2:3], bwd);

    real polynomialEquivalentIndex;
    real polynomialAlpha;

    analog begin
        // Voltage dependency
        polynomialEquivalentIndex = n0 + n1 * groupIndex / refGroupIndex * V(ele_in); // Slow-light enhancement
        polynomialAlpha = a0 + a1 * V(ele_in);

        // Transfer function
        OptE(transfer_pol[0]) <+ exp(- polynomialAlpha / 2 * length); // Propagation loss
        OptE(transfer_pol[1]) <+ (- length * polynomialEquivalentIndex * 2 * `M_PI * `F_REF / `P_C) % (2 * `M_PI); // Phase rotation

        // Output
        OptE(opt_out[0]) <+ absdelay(OptE(fwd[0]), length*groupIndex / `P_C);
        OptE(opt_out[1]) <+ absdelay(OptE(fwd[1]), length*groupIndex / `P_C);
        OptE(opt_in[2]) <+ absdelay(OptE(bwd[0]), length*groupIndex / `P_C);
        OptE(opt_in[3]) <+ absdelay(OptE(bwd[1]), length*groupIndex / `P_C);
    end
endmodule
```

This article has been accepted for inclusion in a future issue of this journal. Content is final as presented, with the exception of pagination.

Listing 6: Verilog-A model of optical reflection (ReflectinInterface.va).

```
module ReflectionInterface(node1, node2);
    inout [0:3] node1;
    inout [0:3] node2;
    optical [0:3] node1, node2;

    parameter real reflection = 0;

    analog begin
        OptE(node1[2]) <+ sqrt(1 - reflection) * OptE(node2[2]) + sqrt(reflection) * OptE(node1[0]);
        OptE(node1[3]) <+ sqrt(1 - reflection) * OptE(node2[3]) + sqrt(reflection) * OptE(node1[1]);
        OptE(node2[0]) <+ sqrt(1 - reflection) * OptE(node1[0]) + sqrt(reflection) * OptE(node2[2]);
        OptE(node2[1]) <+ sqrt(1 - reflection) * OptE(node1[1]) + sqrt(reflection) * OptE(node2[3]);
    end
endmodule
```

Listing 7: Verilog-A model of an EDFA (NoisyEDFA.va).

```
module NoisyEDFA(in, out);
    inout [0:3] in, out;
    optical [0:3] in, out;
    optical [0:1] transfer, transfer_pol, noise_pol, out_tmp, out_tmp_pol, out_pol;

    parameter real gain = 3.0; // [dB]
    integer seed = 52924;
    integer mean = 0;
    real noise_density = 0; // [W/Hz]
    real noise_power = 0; // [W]
    real fs = 5e12;      // sample rate [Hz]

    // EDFA Gain
    Polar2Cartesian Polar2Cartesian1(transfer_pol, transfer);
    CartesianMultiplier CartesianMultiplier1(transfer, in[0:1], out_tmp);

    // ASE Noise
    Cartesian2Polar Cartesian2Polar1(out_tmp, out_tmp_pol);
    CartesianAdder CartesianAdder1(out_tmp_pol, noise_pol, out_pol);
    Polar2Cartesian Polar2Cartesian2(out_pol, out[0:1]);

    analog begin
        @(initial_step) begin
            noise_density = 3.44e-19 * (pow(10, gain / 10) - 1);
            noise_power = noise_density * fs;
        end

        OptE(noise_pol[0]) <+ $rdist_normal(seed, mean, sqrt(noise_power)); // ASE Amplitude
        OptE(noise_pol[1]) <+ 0; // No phase noise
        OptE(transfer_pol[0]) <+ pow(10, gain / 20); // Gain
        OptE(transfer_pol[1]) <+ 0; // No phase rotation

        // Ideal isolation
        OptE(in[2]) <+ 0;
        OptE(in[3]) <+ 0;
    end
endmodule
```

Listing 8: Verilog-A model of the tunable filter (TunableFilter.va).

```
module TunableFilter(in, out);
    inout [0:3] in, out;
    optical [0:3] in, out, in_tmp, out_tmp;
    optical [0:1] osc1, osc2;

    parameter real wavelength = 1551; // [nm]
    real center_freq = `P_C / wavelength / 1e-9; // [Hz]

    // Reference frequency conversion
     CartesianMultiplier CartesianMultiplier1(in[0:1], osc1, in_tmp[0:1]);
    CartesianMultiplier CartesianMultiplier2(out_tmp[0:1], osc2, out[0:1]);

    CartesianMultiplier CartesianMultiplier3(out[2:3], osc1, out_tmp[2:3]);
    CartesianMultiplier CartesianMultiplier4(in_tmp[2:3], osc2, in[2:3]);

    analog begin
        // delta=2nm
        OptE(out_tmp[0]) <+ laplace_nd(OptE(in_tmp[0]), {2.347141585877207e+71,0,0,0,0,0,0}, {2.347141585877208e+71,1.154657487839621e+60,2.840122475453116e+48,4.428868818445329e+36,4.604233134433859e+24,3.034545479782387e+12,1});
        OptE(out_tmp[1]) <+ laplace_nd(OptE(in_tmp[1]), {2.347141585877207e+71,0,0,0,0,0,0}, {2.347141585877208e+71,1.154657487839621e+60,2.840122475453116e+48,4.428868818445329e+36,4.604233134433859e+24,3.034545479782387e+12,1});
        OptE(in_tmp[2]) <+ laplace_nd(OptE(out_tmp[2]), {2.347141585877207e+71,0,0,0,0,0,0}, {2.347141585877208e+71,1.154657487839621e+60,2.840122475453116e+48,4.428868818445329e+36,4.604233134433859e+24,3.034545479782387e+12,1});
        OptE(in_tmp[3]) <+ laplace_nd(OptE(out_tmp[3]), {2.347141585877207e+71,0,0,0,0,0,0}, {2.347141585877208e+71,1.154657487839621e+60,2.840122475453116e+48,4.428868818445329e+36,4.604233134433859e+24,3.034545479782387e+12,1});

        // Local oscillation for the reference frequency converison
        OptE(osc1[0]) <+ cos(-2 * `M_PI * (center_freq - `F_REF) * $abstime);
        OptE(osc1[1]) <+ sin(-2 * `M_PI * (center_freq - `F_REF) * $abstime);
        OptE(osc2[0]) <+ cos(2 * `M_PI * (center_freq - `F_REF) * $abstime);
        OptE(osc2[1]) <+ sin(2 * `M_PI * (center_freq - `F_REF) * $abstime);
    end
endmodule
```

ACKNOWLEDGMENT

This work was supported through the activities of VDEC, The University of Tokyo, in collaboration with Keysight Technologies, Inc. and Cadence Design Systems, Inc. The authors thank Dr. Mikiya Kamata for the modulator design and Dr. Takemasa Tamanuki for technical advice on the EDFA evaluation.

This article has been accepted for inclusion in a future issue of this journal. Content is final as presented, with the exception of pagination.

REFERENCES

[1] 400G-FR4 Technical Specification, 100G Lambda MSA Group, Sep. 2018. [Online]. Available: https://www.100glambda.com/specifications/download/2-specifications/7-400g-fr4-technical-spec-d2p0

[2] K. Li et al., "An integrated CMOS–silicon photonics transmitter with a 112 gigabaud transmission and picojoule per bit energy efficiency," *Nature Electron.*, vol. 6, no. 11, pp. 910–921, Oct. 2023, doi: 10.1038/s41928-023-01048-1.

[3] P. -H. Chang et al., "A 3D integrated energy-efficient transceiver realized by direct bond interconnect of co-designed 12 nm FinFET and silicon photonic integrated circuits," *J. Lightw. Technol.*, vol. 41, no. 21, pp. 6741–6755, Nov. 2023.

[4] C. S. Levy et al., "8-λ × 50 gbps/λ heterogeneously integrated si-ph DWDM transmitter," *IEEE J. Solid-State Circuits*, vol. 59, no. 3, pp. 690–701, Mar. 2024, doi: 10.1109/JSSC.2023.3344072.

[5] K. Kawahara and T. Baba, "DAC- and DSP-free optical transmitter based on triple-parallel Si Mach-Zehnder modulators," in *Proc. IEEE Silicon Photon. Conf.*, 2024, pp. 1–2, doi: 10.1109/SiPhotonics60897.2024.10544370.

[6] K. Kawahara, T. Tsuchizawa, N. Yamamoto, Y. Maegami, K. Yamada, and T. Baba, "59-fJ/bit Si photonic crystal slow-light modulator with FinFET-compatible driving voltage," in *Proc. Opt. Fiber Commun. Conf. Exhib.*, 2024, pp. 1–3.

[7] K. Kawahara et al., "1.9-pJ/bit 0.5-mm^2 high-speed optical transmitter including silicon slow-light modulator and current-mode BiCMOS driver," in *Proc. 50th Eur. Conf. Opt. Commun.*, 2024, pp. 778–781.

[8] K. Kawahara et al., "High-speed, low-voltage, low-bit-energy silicon photonic crystal slow-light modulator with impedance-engineered distributed electrodes," *Optica*, vol. 11, no. 9, pp. 1212–1219, Sep. 2024, doi: 10.1364/OPTICA.531372.

[9] Verilog-AMS Language Reference Manual, Accellera, 2024. [Online]. Available: https://www.accellera.org/downloads/standards/v-ams

[10] E. Kononov, "Modeling photonic links in verilog-A," M.E. thesis, Dept. Elect. Eng. Comput. Sci., Massachusetts Inst. Technol., Cambridge, MA, USA, 2013. [Online]. Available: https://dspace.mit.edu/handle/1721.1/85432

[11] C. M. Sorace-Agaskar, "Analog integrated photonics," Ph.D. dissertation, Dept. Elect. Eng. Comput. Sci., Massachusetts Inst. Technol., Cambridge, MA, USA, 2015. [Online]. Available: https://dspace.mit.edu/handle/1721.1/97812

[12] C. Sorace-Agaskar et al., "Electro-optical co-simulation for integrated CMOS photonic circuits with VerilogA," *Opt. Exp.*, vol. 23, no. 21, pp. 27180–27203, Oct. 2015, doi: 10.1364/OE.23.027180.

[13] M. J. Shawon and V. Saxena, "Rapid simulation of photonic integrated circuits using Verilog-A compact models," in *Proc. IEEE 62nd Int. Midwest Symp. Circuits Syst.*, 2019, pp. 424–427, doi: 10.1109/MWSCAS.2019.8885372.

[14] M. J. Shawon and V. Saxena, "Rapid simulation of photonic integrated circuits using Verilog-A compact models," *IEEE Trans. Circuits Syst. I, Reg. Papers*, vol. 67, no. 10, pp. 3331–3341, Oct. 2020, doi: 10.1109/TCSI.2020.2983303.

[15] E. de Foucauld, O. Rozeau, A. Myko, D. Fowler, L. Virot, and F. Gays, "Compact modeling of photonic devices in Verilog-A for integrated circuit design," *Solid-State Electron.*, vol. 200, Feb. 2023, Art. no. 108538, doi: 10.1016/j.sse.2022.108538.

[16] H. Fang et al., "Accurate time-domain and frequency-domain co-simulation approach for OEICs design with Verilog-A," *Opt. Exp.*, vol. 32, no. 2, pp. 1764–1775, Jan. 2024, doi: 10.1364/OE.510277.

[17] D. Ming, Y. Wang, Z. Wang, K. X. Wang, C. Qiu, and M. Tan, "EPHIC models: General SPICE photonic models for closed-loop electronic-photonic co-simulation," *IEEE Trans. Circuits Syst. I, Reg. Papers*, vol. 71, no. 4, pp. 1819–1831, Apr. 2024, doi: 10.1109/TCSI.2024.3353459.

[18] Y. Ye, D. Spina, W. Bogaerts, and T. Dhaene, "Baseband macromodeling of linear photonic circuits for time-domain simulations," *J. Lightw. Technol.*, vol. 37, no. 4, pp. 1364–1373, Feb. 2019, doi: 10.1109/JLT.2019.2893545.

[19] Y. Ye et al., "Time-domain compact macromodeling of linear photonic circuits via complex vector fitting," *Photon. Res.*, vol. 7, no. 7, pp. 771–782, Jul. 2019, doi: 10.1364/PRJ.7.000771.

[20] J. Feng, F. Zhao, and Y. Ye, "Extracting causal impulse responses from baseband band-limited S-parameters of passive photonic integrated circuits for time-domain simulations," *Opt. Exp.*, vol. 32, no. 5, pp. 7697–7709, Feb. 2024, doi: 10.1364/OE.507238.

[21] X. Jiang and Y. Ye, "Incorporating frequency responses of passive photonic integrated circuits into discrete time-domain simulations using pole-residue fitting," *Opt. Laser Technol.*, vol. 175, Aug. 2024, Art. no. 110718, doi: 10.1016/j.optlastec.2024.110718.

[22] K. Yue and Y. Ye, "Efficient Verilog-A based time-domain variability analysis method for passive photonic integrated circuits," *Opt. Exp.*, vol. 32, no. 11, pp. 18493–18507, May 2024, doi: 10.1364/OE.520287.

[23] J. Rhim, Y. Ban, B.-M. Yu, J.-M. Lee, and W.-Y. Choi, "Verilog-A behavioral model for resonance-modulated silicon micro-ring modulator," *Opt. Exp.*, vol. 23, no. 7, pp. 8762–8772, Apr. 2015, doi: 10.1364/OE.23.008762.

[24] B. Wang et al., "A compact Verilog-A model of silicon carrier-injection ring modulators for optical interconnect transceiver circuit design," *J. Lightw. Technol.*, vol. 34, no. 12, pp. 2996–3005, Jun. 2016, doi: 10.1109/JLT.2015.2505239.

[25] K. Zhu, V. Saxena, X. Wu, and W. Kuang, "Design considerations for traveling-wave modulator-based CMOS photonic transmitters," *IEEE Trans. Circuits Syst. II, Exp. Briefs*, vol. 62, no. 4, pp. 412–416, Apr. 2015, doi: 10.1109/TCSII.2014.2387682.

[26] K. Zhu, R. Wang, X. Wu, and V. Saxena, "Behavioral modeling and characterization of silicon photonic Mach-Zehnder modulator," in *Proc. IEEE 60th Int. Midwest Symp. Circuits Syst.*, 2017, pp. 989–992, doi: 10.1109/MWSCAS.2017.8053092.

[27] H. A. R. Rivera, M. van Niekerk, and S. F. Preble, "Silicon photonic optical-electrical-optical modulator neuron Verilog-A model," in *Proc. 2021 Conf. Lasers Electro-Opt.*, 2021, pp. 1/2.

[28] Q. Liu et al., "High-power micro-ring modulator and multi-channel coupled ring resonator for WDM design on a 300-mm monolithic foundry platform," in *Proc. Opt. Fiber Commun. Conf. Exhib.*, 2024, pp. 1–3.

[29] Jun. 2025. [Online]. Available: https://github.com/keikawa/Verilog-A-photonic-model-library

[30] L. Marple, "Computing the discrete-time 'analytic' signal via FFT," *IEEE Trans. Signal Process.*, vol. 47, no. 9, pp. 2600–2603, Sep. 1999, doi: 10.1109/78.782222.

[31] M. Wang, A. Ribero, Y. Xing, and W. Bogaerts, "Tolerant, broadband tunable 2 × 2 coupler circuit," *Opt. Exp.*, vol. 28, no. 4, pp. 5555–5566, Feb. 2020, doi: 10.1364/OE.384018.

[32] W. R. Eisenstadt and Y. Eo, "S-parameter-based IC interconnect transmission line characterization," *IEEE Trans. Compon., Hybrids, Manuf. Technol.*, vol. 15, no. 4, pp. 483–490, Aug. 1992, doi: 10.1109/33.159877.

[33] Y. Terada, H. Ito, H. C. Nguyen, and T. Baba, "Theoretical and experimental investigation of low-volgage and low-loss 25-Gbps Si photonic crystal slow light Mach–Zehnder modulators with interleaved p/n junction," *Front. Phys.*, vol. 2, 2014, Art. no. 61.

[34] Y. Hinakura, H. Arai, and T. Baba, "64 Gbps Si photonic crystal slow light modulator by electro-optic phase matching," *Opt. Exp.*, vol. 27, no. 10, pp. 14321–14327, May 2019, doi: 10.1364/OE.27.014321.

[35] A. Yariv and P. Yeh, *Photonics: Optical Electronics in Modern Communication*, 6th ed. New York, NY, USA: Oxford Univ. Press, 2006, ch. 17.

[36] J. Spurlock, "Improving VNA measurement accuracy with quality cables and adapters," Jul. 2017. Accessed: Feb. 16, 2023. [Online]. Available: https://www.tek.com/en/blog/improving-vna-measurement-accuracy-quality-cables-and-adapters

[37] J. C. Liu and K. Wong, "Test port cable instability and VNA measurement errors," in *Proc. 81st ARFTG Microw. Meas. Conf.*, Seattle, WA, USA, 2013, pp. 1–8, doi: 10.1109/ARFTG.2013.6579032.

[38] K. Kawahara et al., "High efficiency compact optical transmitter with a total bit energy of 0.78 pJ/bit including silicon slow-light modulator and open-collector current-mode driver," to be published.

This article has been accepted for inclusion in a future issue of this journal. Content is final as presented, with the exception of pagination.



KEISUKE KAWAHARA (Member, IEEE) received the B.E. and M.E. degrees in engineering from Tokyo University of Science, Chiba, Japan, in 2020 and 2022, respectively, and the Ph.D. degree in engineering from Yokohama National University, Yokohoma, Japan, in 2025. He is currently an Assistant Professor with the Institute of Science Tokyo, Bunkyō, Japan. His research interests include electronic and photonic integrated circuits. Dr. Kawahara is a member of Optica, SPIE, IEICE, and JSAP. He was the recipient of the IEEE MTT-S Japan Chapter Young Engineer Award in 2024, JSAP Young Scientist Presentation Award in 2024, and IEICE Young Researcher's Award in 2022.



TOSHIHIKO BABA (Fellow, IEEE) received the B.E., M.E., and Ph.D. degrees from the Division of Electrical and Computer Engineering, Yokohama National University, Yokohama, Japan, in 1985, 1987, and 1990, respectively. He was an Associate Professor and Full Professor with Yokohama National University, in 1994 and 2005, respectively. He has studied ARROW waveguides, VCSELs, micro/nano lasers and spontaneous emission control, photonic crystals, Si photonics, slow light, biosensors, optical modulators, and LiDAR. He is a Fellow Member of JSAP and Optica, as well as an Associate Member for the Science Council of Japan. He was the Vice President of JSAP during 2018–2020. He was the recipient of the JSPS Prize in 2006, IEEE/LEOS Distinguished Lecturer from 2006 to 2007, Commendation for Science and Technology by the MEXT in 2016, and Medal of Purple Ribbon in 2024.